Investigation of the Foaming Process of Metals by Synchrotron-Radiation Imaging

L. Helfen[*a,b], H. Stanzick[c], J. Ohser[d], K. Schladitz[d], P. Rejmánková-Pernot[a,b], J. Banhart[e] and T. Baumbach[a,b]

[a] Fraunhofer Institute for Nondestructive Testing (IZFP), EADQ, D-01326 Dresden, Germany

[b] European Synchrotron Radiation Facility, BP 220, F-38043 Grenoble Cedex, France

[c] Fraunhofer Institute for Manufacturing and Advanced Materials (IFAM), D-28359 Bremen, Germany

[d] Fraunhofer Institute for Industrial Mathematics (ITWM), D-67663 Kaiserslautern, Germany

[e] Hahn-Meitner-Institut, D-14109 Berlin, Germany

ABSTRACT

Synchrotron-radiation imaging serves as a powerful tool for the non-destructive material characterisation of metallic foams. The foaming process is visualised *in situ* by real-time radiography in projection image sequences. The temporal evolution of foam expansion from early pore formation over pore growth up to the collapse of the foam structure are reported. *Ex situ* microtomography is applied for the study of statistical distribution properties at the early foaming stages.

Various image processing and analysis techniques yield quantitative results concerning pore nucleation and their early formation, film rupture and foam drainage. The similarities and differences of the metal foaming process with respect to the precursor material, its processing steps and process parameters are determinable.

Keywords: metal foam, non-destructive testing, synchrotron radiation, *in situ* radiography, computerised tomography, 3d image processing and analysis

1. INTRODUCTION

Metallic foams are modern microstructured materials which are interesting for technological application as solid foams. Due to relative densities $\eta = \rho_{\mathrm{por}}/\rho_{\mathrm{s}}$ (where ρ_{por} is the macroscopically determined mass density of the porous foam and ρ_{s} is the theoretical bulk density of the solid precursor material) up to a factor of one sixth, light-weight construction is one of the main interests for the application of metallic foams, especially in the case of aluminium alloy foams. Moreover, the high energy dissipation per unit mass makes those foams attractive in ground transportation applications for increasing passenger safety in crash situations. Additionally, improved properties with respect to the bulk materials concerning acoustical and mechanical damping and heat conduction may be noted.[1]

Depending on foam expansion, metallic foams can have characteristic sizes and distances of their constituents on and below the micrometre scale. Modern x-ray laboratory computerised tomography (CT) scanners are able to attain spatial resolutions down to approximately 10 μm which allows one to resolve the cell walls of aluminium alloy foams and thus to study the 3D structure[2] of expanded metal foams, *e.g.* under mechanical load.[3] Olurin *et al.*[4] acquired 3D data to determine morphological parameters of foam samples near full expansion.

Although nowadays the technology for metal foaming is rather well established, metal foam *formation* is still rather poorly explored. In this paper we demonstrate the application of SR imaging to investigate metal foam formation. High spatial resolutions presently down to approximately 1 μm can be attained for the investigation of small spatial features. The application of SR for non-destructive material characterisation is also favourable[5] with respect to a high beam intensity per unit solid angle, monochromatic radiation which avoids the effects of beam hardening and phase contrast[6, 7] due to coherent illumination.

* Email: helfen@esrf.fr

In situ observation of the foaming process under thermal load is performed by radiographic experiments. They were the first experiments which allowed the study of the internal foam structure during expansion under heat treatment. Some results concerning foaming physics, the materials science aspects and concerning technological application have already been described elsewhere.[8–10] In this paper, selected two-dimensional (2d) image analysis techniques are applied to yield quantitative results concerning foam drainage and bubble collapse.

Especially at early foaming stages, small spatial features (such as small pores) cannot be distinguished in the projection images since they are superposed. In order to avoid the confusion of superposition, CT is applied to various sample series in which each sample represents a particular expansion stage corresponding to a certain foaming time. Three-dimensional (3d) image analysis techniques are used to quantify distribution properties of the 3d microstructure of such partly expanded foam samples. The comparison between the individual samples of the series yields a description of pore nucleation and their early formation. Further results obtained by different image analysis techniques are published elsewhere.[11]

The samples investigated in this paper are mostly fabricated by the *powder metallurgical* (PM) method[1] which is described in Sect. 2.1. In Sects. 2.2 and 2.3 follow the two experimental set-ups which have been employed for *in situ* radiography and *ex situ* microtomography. Then in Sect. 3 we present results obtained by the experiments and by the applied image processing and analysis techniques. The final conclusions in Sect. 4 subsume the results.

2. SAMPLES AND EXPERIMENTAL SET-UPS

2.1. Sample preparation

Nowadays there exists a variety of methods[1,12] for metal foam fabrication. The two-step procedure of the PM fabrication method is described in the following for a foam made of an aluminium alloy containing 7 wt-% of silicon (AlSi7).

For the *fabrication of a foamable precursor* three powders were used, namely powders of pure aluminium and of pure silicon to form an AlSi7 alloy matrix with the addition of 0.5 wt-% of a TiH_2 powder as the blowing agent. Subsequently, the powder blend was compacted to a foamable precursor material by conventional axial (closed-die) compression at a temperature of 450 °C and a pressure of 120 MPa. The resulting precursor material is virtually dense (≤ 0.75 % porosity).[8] Extrusion would be an alternative powder compaction method[13] which is especially suited for industrial application.

For the *fabrication of the final metal foam*, the foaming process is triggered by heating the obtained precursor material within a pre-heated furnace. During the heating process the blowing agent TiH_2 decomposes and releases the blowing gas hydrogen. As a consequence pores form in the metal matrix and the sample expands. Furnace temperatures between 600 and 800 °C are usually employed for foaming Al alloys. Highest volume expansion during foaming can be expected at around 700 °C for AlSi7 precursor materials with 0.5 wt-% TiH_2.[13] For technological application the foaming process is interrupted at its maximum expansion by quenching the sample, freezing in this way the foam structure.

Instead of the two base powders Al and Si forming the alloy we also use (as in the case of AA6061) one *pre-alloyed* powder or (as in the case of Zn) one powder of an *elemental* metal. Pre-alloyed powders are more expensive and therefore less employed for technological applications. Moreover, pre-alloyed AlSi alloy powders were found to exhibit a significantly worse foamability[14] than their counterpart based on two base powders.

2.2. *In situ* real-time radiography

For the observation of the foaming process by *in situ* x-ray imaging experiments, a specially designed furnace was integrated into the beam path of beamline ID19 at the ESRF (see Fig. 1). To allow the x-ray beam to pass through the furnace, highly polished Al windows cooled by water were used in its construction. The white synchrotron beam was monochromatised to 33.2 keV for Al foaming and 70 keV for Zn foaming by choosing a suitable diffraction peak (Si 111) within the horizontal plane around the Si monochromator crystal (in transmission geometry). The furnace was mounted to rotate around the monochromator crystal in the horizontal plane and installed on a sideward translation permitting the beam to pass through its centre where the sample could be moved to by a motorised vertical translation. By passing the monochromatic beam through the sample placed within the furnace, an absorption radiograph could be acquired by the electronic detector system based on a charge-coupled device (CCD) chip (ESRF Frelon camera). In combination with interchangeable light-optical units, effective pixel sizes of down to 10 μm could be realised.

For low temporal resolutions, the CCD was read out steadily with constant exposure times of 0.3 or 0.5 s resulting in image frequencies between 2 and 3 Hz. The entire foaming experiments took a few minutes, corresponding to a sequence

of between 500 and 900 radiographs for each of the more than 200 individual experiments carried out. Additionally, a dedicated operation mode of the ESRF Frelon 2000 camera was applied for obtaining peak frame rates of up to 18 Hz. Using this operation mode, a region of the CCD serves for image exposure, the remaining non-exposed surface is reserved for image storage. After exposure the electric charge can be shifted quickly to the reserved non-exposed region. In this way, a fast series of four images could be acquired and stored on the CCD. Exposure times in the order of 50 ms and a vertical image size of 256 lines (and 2048 pixel horizontal width) translating into a shift time of approximately 5 ms were realised.

2.3. *Ex situ* microtomography

On the right-hand side of Fig. 1, a typical set-up used at ID19 for microtomography is sketched. The basic elements are the synchrotron source (at approx. 140 m distance, not shown), a double-crystal monochromator, a rotation stage employed to turn the sample during the tomographic scan and the detector.

The low beam divergence available at synchrotron sources permits the use of monochromator optics. Monochromatic radiation enables the quantitative reconstruction of the spatial distribution of the linear attenuation coefficient $\mu(x, y, z)$ for the selected x-ray energy, avoiding artefacts due to beam hardening. As a consequence the visibility of spatial features in the reconstructed image is improved for the identification of the blowing agent particles, alloy matrix and pores. For intermediate pixel sizes from approximately 5 μm onwards we usually employ the fixed-exit double-crystal monochromator with its 111 reflection of prefect silicon crystals. For higher imaging resolutions down to pixel sizes of 0.3 μm we use a high-bandwith multilayer monochromator diffracting in a vertical plane.

3. EXPERIMENTAL RESULTS AND IMAGE ANALYSIS

3.1. *In situ* real-time radiography

With the experimental set-up described in Sect. 2.2 foams could be produced and observed by the synchrotron x-ray beam. For each sample a series of digital radiographs was acquired for monitoring the foaming process. Fig. 2 shows in each column six full-field radiographs of an expanding foam sample in different stages of evolution. The samples are heated up in the pre-heated furnace causing the release of hydrogen gas by the blowing agent which has been compacted into the precursor material. We define the foaming time $t = 0$ as the onset of sample expansion, as visible from the radiographic image sequence. The various evolution steps can be divided into two phases: in "I" the first four frames show the samples rising from their initial height to maximum expansion, "II" marks the last three frames with expanded foams of almost constant volume in which internal processes lead to changes in the bubble structure.

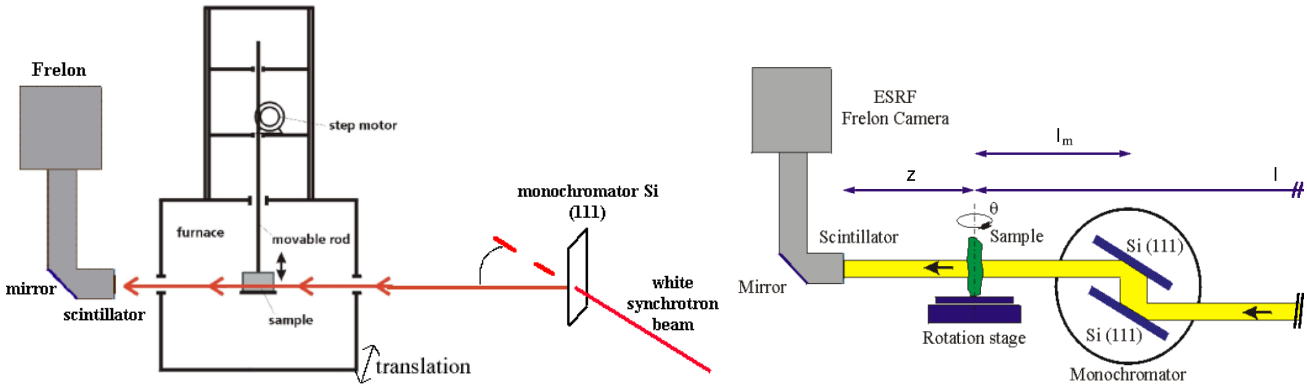

Figure 1. Sketches of the experimental set-ups used for *in situ* real-time radiography (left) and microtomography (right) at the beamline ID19 of the ESRF. Both schemes show the set-up between monochromator and detector, where l_m ist the distance between sample and monochromator. The source is a multiple of this distance away from the monochromator (*e.g.* $l_m \approx 5$ m, $l \approx 145$ m in the case of beamline ID19). In both set-ups we use the ESRF Frelon CCD camera as a basis for the electronic detector system. Different effective pixel sizes of the acquired image can be realised by changing the optics unit composed by a scintillator screen or crystal, a visible-light magnifying or demagnifying optics system and a mirror.

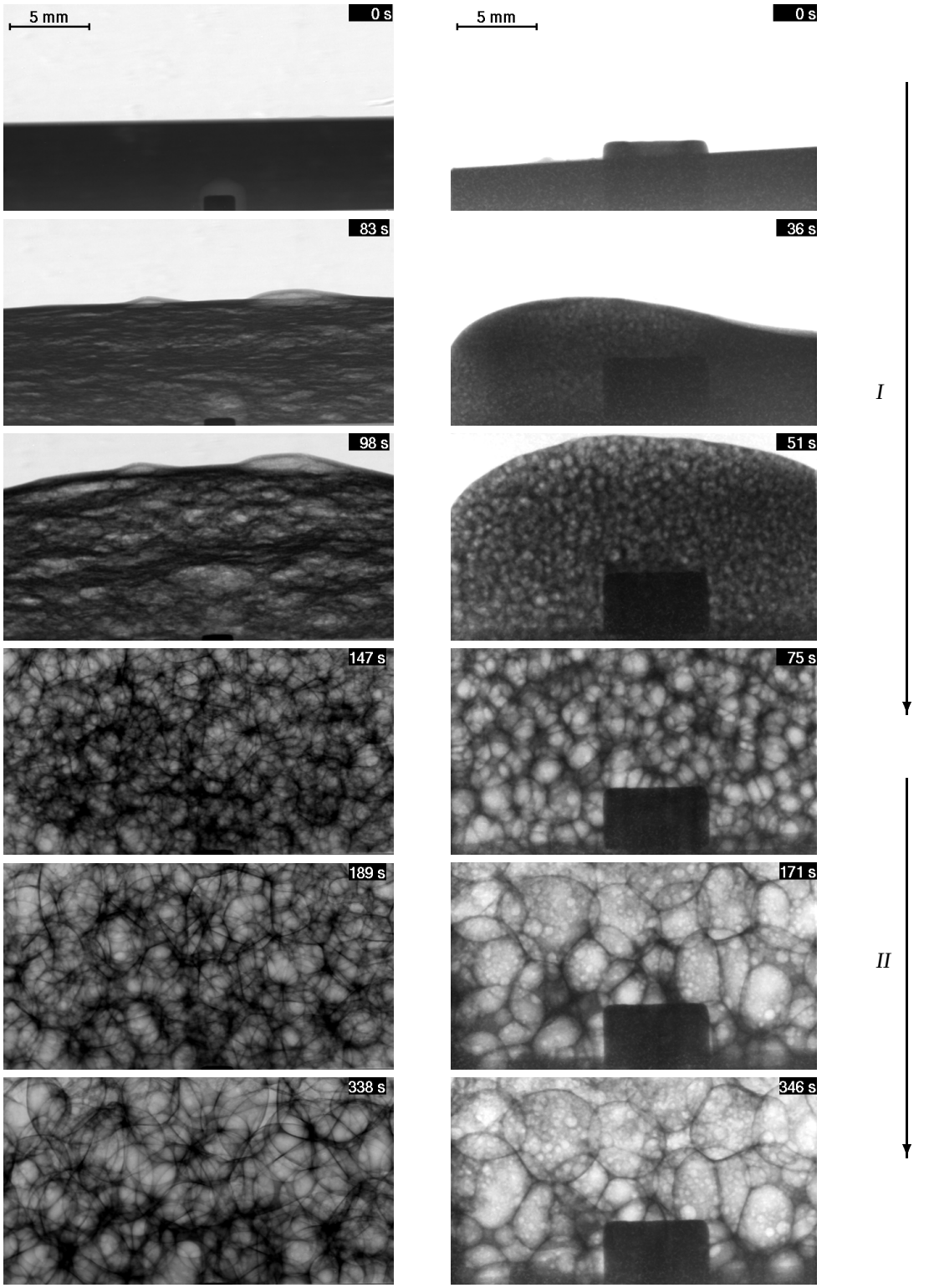

Figure 2. Series of expansion stages of an AlSi7 alloy foam (left column) and a Zn foam within a foaming mould (right column), monitored by x-ray radiography. The original samples (top frame) were $d = 10$ mm and $d = 7$ mm thick (x-ray energies 33.2 and 70.0 keV), respectively. In frames 4 to 6 both foams have risen to more than 15 mm height and are therefore truncated. "I" marks phases of rising foam and "II" stages of decaying foam at nearly constant volume. The times given refer to a state at which expansion started, *i.e.* after about 120 s for AlSi7 and 240 s for Zn after inserting the sample into the pre-heated furnace. Furnace temperatures were 700 and 525 °C, respectively. In the case of Zn, the black static pattern at the bottom of each frame is a screw which supports the mould.

For AlSi7 (left column), the melting temperature range (577 to 620 °C) lies well above the decomposition range of the blowing agent which starts[13] in the case of free TiH_2 between 380 and 400 °C at ambient pressure. As can be seen in phase "I" this leads to the formation of thin fissures rather than round pores. The pores round off as the metal foam expands and finally become fairly equiaxed after about 120 s. The direction of foam rise is always parallel to the short axis of the voids which in turn is parallel to the pressing direction of the powder mix. Therefore, the texture created during compaction (uniaxial compression) of the powders must be responsible for this anisotropy. Looking at phase "II", first we see that the foam structure gets coarser with time and there is a slight tendency for metal flowing downwards under the influence of gravity. This drainage effect, however, is much less pronounced than in most aqueous foams. Only an increase of the furnace temperature to at least 750 °C in further experiments led to considerable drainage. Analysis of the entire image sequence reveals[8] that spontaneous metal film rupture is the sole mechanism for coalescence* and that there is no sign for gradual gas diffusion between the cells.

For comparison, the right column of Fig. 2 shows a selection of six full-field radiographs of a Zn foam (with ZrH_2 as blowing agent) at similar expansion stages as for AlSi7. Again, the fourth frame corresponds to maximum expansion, after which there is no more height increase taking place. The most obvious difference is that for Zn from the very beginning of foaming the pores are round in shape. In the case of Zn, pore nucleation takes place in analogy with aqueous foams since the metal begins to melt (420 °C) when the blowing agent ZrH_2 starts to release its hydrogen. Therefore, the released hydrogen gas causes the nucleation of round pores.

3.1.1. High temporal resolution

The experiments carried out with a high temporal resolution open up the possibility to investigate fast processes. An example is given in Fig. 3 for an AlSi7 foam at a relatively high furnace temperature of $T = 775\,°C$. The left column shows a sequence of acquired radiographs, the right column the difference image between two successive frames in the left column. The difference images facilitate the detection of changes between two images: vanishing metal is shown in white in the difference images (right column), appearing metal in black. In this way, gradual film rearrangements are visible as black-white contrasted lines whereas ruptures are discernible as larger areas with light contrast (where metal disappeared) and dark contrast (where metal appears). Arrows highlight film rupture events and other changes.

The collapse of a large bubble on the right hand side of the first radiograph (just before the arbitrarily defined $t = 0$) is followed by a succession of film rearrangements and film ruptures. Over two subsequent frames ($t = 0$ and $t = 55$ ms) a bubble at the bottom border of the radiographs vanishes and films in the centre rearrange (see arrows in the corresponding difference images). Then, in frame $t = 110$ ms a film ruptures, followed again by film rearrangements (see black-white contrasted lines in the difference images up to $t = 415$ ms. Finally, at $t = 525$ ms a small bubble at the bottom of the frame disappears.

We see that it is possible to examine the reorganisation procedures taking place during foaming. The fast succession of rupture events suggests a causal connexion between them: if films get stretched too much — as caused by the large-scale collapse event between $t = -250$ ms and $t = 0$ — they become unstable and rupture. The rupture process itself takes less than 50 ms since in no case any sign of a smeared out cell wall has been observed. In the case of Al alloy foams, the critical thickness of metal films just before rupture has been determined[10] to approximately 50 μm.

3.1.2. Drainage

Drainage is the downward flow of liquid through a freshly fabricated foam due to gravity until an equilibrium is attained. Quantification of drainage is performed by an image processing approach which is based on the uniformity of the foaming process with respect to the plane perpendicular to the vertical coordinate h: if over a sufficiently large region at a given h the average density of the foam is determined, characteristic variations of the foam density should appear and quantify drainage in the liquid metal foam.

With monochromatic radiation, beam hardening is avoided so that a calibration of the x-ray transmission with respect to the transversed material thickness is not necessary. If we consider at any foaming time t all points of a given horizontal

*Since with the expression "coarsening" one usually refers[15] to a structural change due to gas diffusion we employ the commonly used expression "coalescence" for the observed collapse due to film rupture.

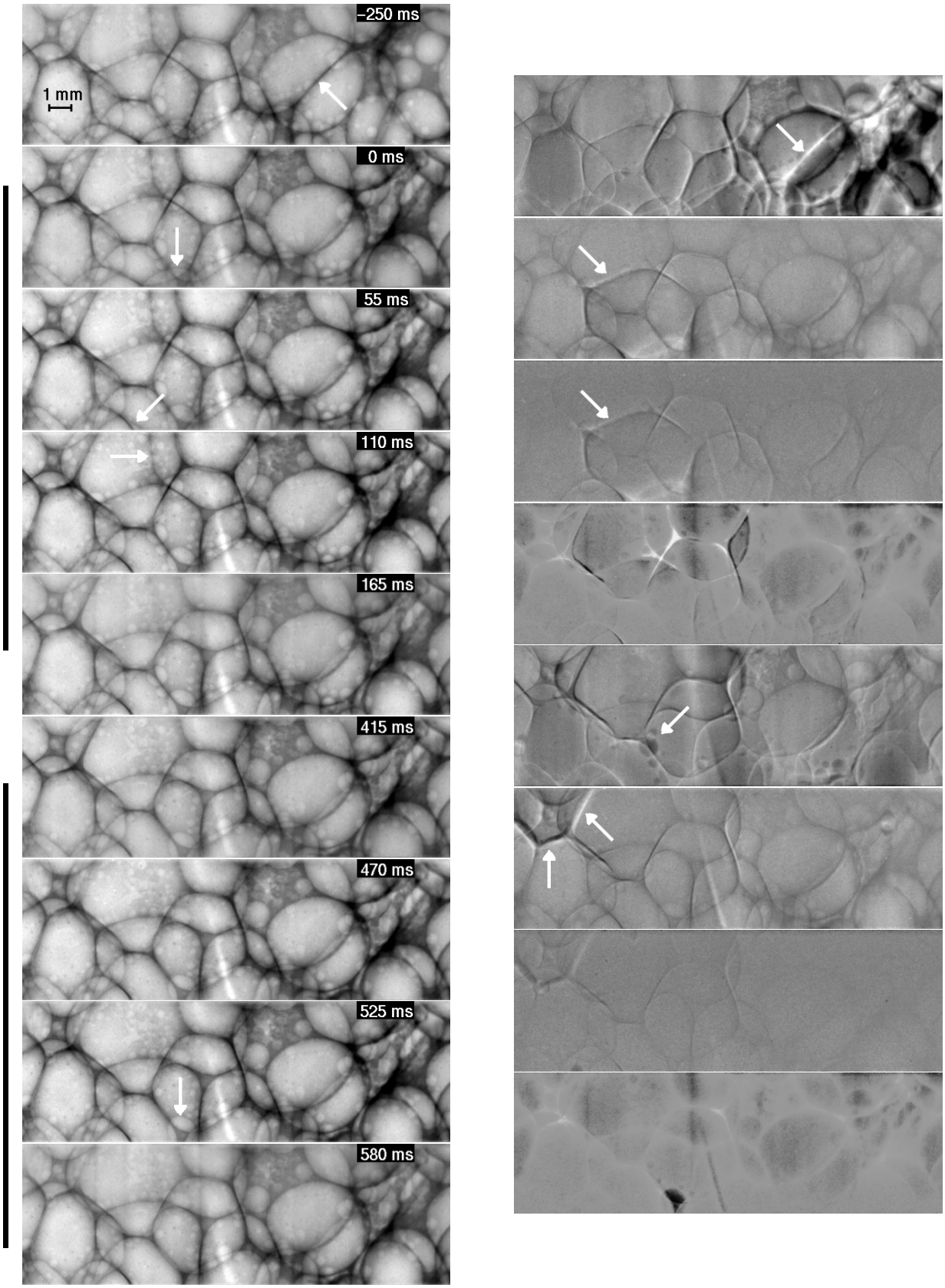

Figure 3. Fast radiography: The disappearance of the large bubble just before time $t_0 = 0$ is followed by a succession of topological rearrangements. The vertical lines mark sets of frames which have been accumulated on the CCD and read out at once. The difference images between two frames (right column, with time intervals of 250 ms between two frame sets) show the rearrangement of the liquid metal. Pixel size is 30 μm, furnace temperature 775 °C.

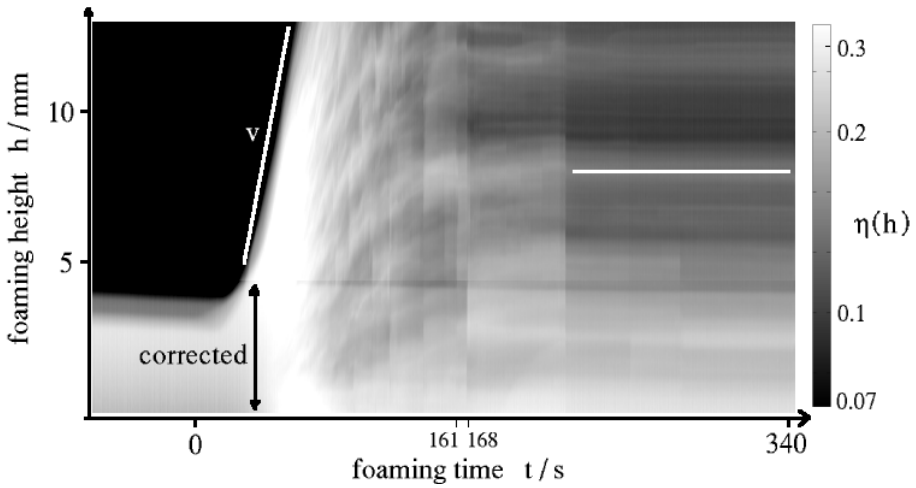

Figure 4. Line-wise integration (according to Eq. (1)) of the acquired images of a Zn foam expanding in an Al mould. A selection of radiographic images for this sample is shown in Fig. 2. The almost horizontal artefact (at the top of the corrected vertical region) stems from an incomplete suppression of the absorption caused by the mould screw. The sample thickness was limited during foaming to $d = 7$ mm by the mould. The times on the ordinate refer to a state at which expansion started which was about 240 s after inserting the sample into the pre-heated furnace set to 525 °C.

plane at height h to show statistically the same characteristic foaming properties (since gravity acts perpendicular to it) we can determine the average (relative) foam density $\eta(h) = \rho(h)/\rho_\mathrm{s}$ (with ρ_s according to the introduction)

$$\eta(h) = \frac{1}{bd}\int_0^b\int_0^d \frac{\mu(x,y,h)}{\mu_\mathrm{s}}\mathrm{d}x\mathrm{d}y = \frac{1}{bd\mu_\mathrm{s}}\int_0^b -\ln T(y,h)\mathrm{d}y\ , \tag{1}$$

where T is the x-ray transmission downstream of the sample, μ_s is the linear attenuation coefficient of the bulk precursor material at the respective x-ray energy, d the sample thickness (limited by the mould) and the integration along y is performed over the entire observed horizontal region $[0 \ldots b]$ (usually limited by beam or detector size). An example is given in Fig. 4 where every digital radiograph of the Zn sample already presented in Fig. 2 is integrated according to Eq. (1), applied to the (discrete) pixel images. By aligning all columns for every point in time on the ordinate, changes of the average density as a function of the foam height (in the vertical direction of the images in Fig. 2) become visible.

At foaming time $t = 0$, the foam starts to expand quickly (see Fig. 4). Porosity is seen from the change of the formerly light grey sample towards darker grey values. The steep line (letter "v") indicates the rising velocity $v = \mathrm{d}h_\mathrm{max}/\mathrm{d}t$ of the foam front. From a foaming time of about 40 s onwards we see the appearance of grey contrasted lines stemming from a local ordering of bubbles and metal films during foam expansion. With proceeding foaming time we clearly see the accumulation of liquid metal at the bottom ($h \approx 0$). This accumulation is not a contiuous process, however: there are strong discontinuities visible along the horizontal direction. These discontinuities stem from film rupture events at the respective foaming times where large bubbles collapse. At the beginning of the foaming process (80 s $\leq t \leq$ 170 s) these rupture events are rather frequent whereas for $t \geq 170$ s the foam structure is rather stable (cf. horizontal white line). It may be concluded that metallic foams are rather unstable so that on the investigated foam volume ($35 \times 14 \times 7$ mm^3) a continuous global drainage is negligible compared to the *pulsed drainage* which occurs locally after film rupture events when the rupture-liberated liquid drains downwards.

3.2. *Ex situ* microtomography

The experimental set-up described in Sect. 2.3 is used to acquire the projection data of a tomographic scan. Reconstruction of the 3d distribution of the linear attenuation coefficient $\mu(x,y,z)$ is performed by a filtered-backprojection algorithm.[16]

Fig. 5 gives an impression of the spatial resolution and image quality realisable by SR microtomography. Two reconstructed slices with 0.7 μm pixel size show different precursor materials shortly after the onset of foaming, *i.e.* with porosities $\varepsilon < 0.1$.[†] Pores are rendered black, alloy matrix in dark grey and highly absorbing blowing agent particles in

[†]The porosity $\varepsilon = 1 - \eta$ is used in the following as a measure to describe the expansion stage.

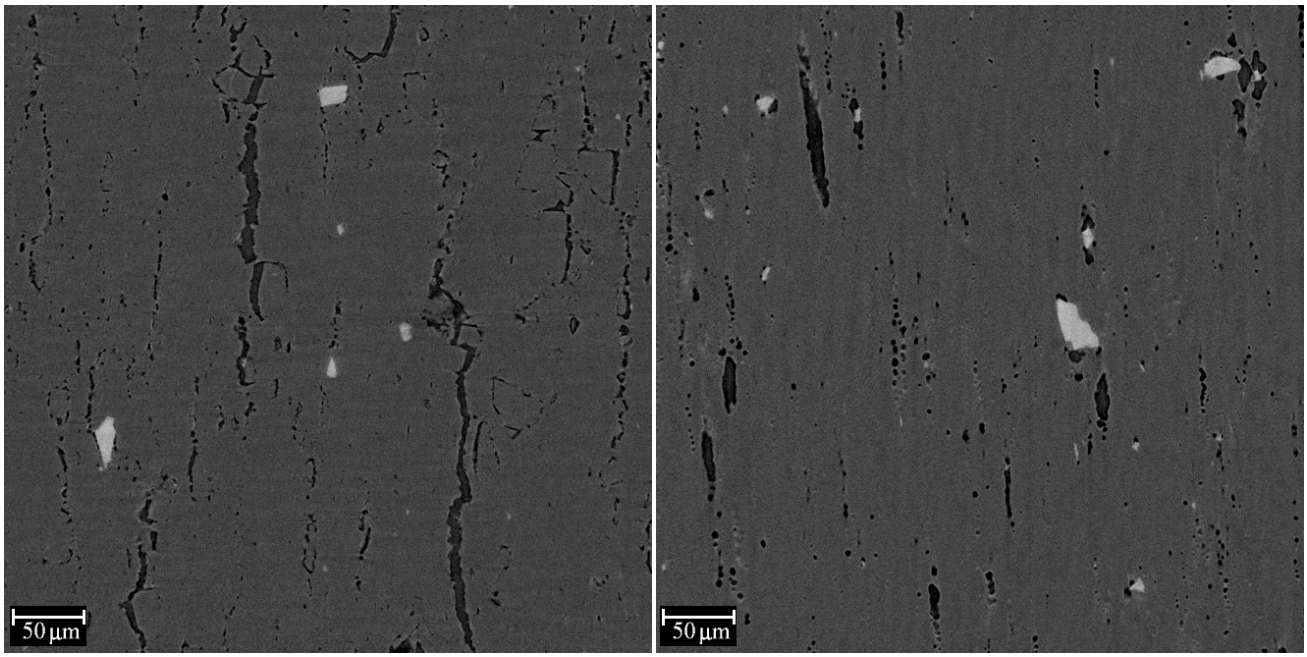

Figure 5. *Ex situ* microtomography: Representative slices taken from the reconstructed 3d data sets. X-ray energy was 18 keV, image sizes are 660×660 voxels of $0.7 \times 0.7\ \mu\text{m}^2$ size. The AlSi7 sample (left, $\varepsilon = 0.09$) stems from a uniaxially compacted mix of Al and Si base powders whereas the AA6061 sample (right, $\varepsilon = 0.01$) is extruded from a pre-alloyed metal powder.

light grey. In both reconstructed slices, the principal compaction direction (of the powder mix) is oriented horizontally. The pore morphology is quite different between the two materials: for AlSi7, irregular crack-like voids are observed whereas for AA6061 they are more regularly shaped. Moreover, for AlSi7 the blowing agent particles do not seem to be spatially correlated with the pores whereas for AA6061 they are often found close to the pores. The choice of the 2d slice through the 3d volume, however, might not cut a pore which is adjacent to a blowing agent particle or *vice versa*. Therefore, by dedicated 3d image processing and analysis techniques, pore morphology and the spatial correlation between pores and blowing agent particles will be investigated in the following.

3.2.1. Evolution of pore morphology

The 3d renditions given in the right column of Fig. 6 visualise the change of the morphology of the pore structure during foam expansion. Already in the solid state, fissure-like pores form up in the metallic matrix. The fissures are spatially extended perpendicular with respect to the principal powder compaction axis. This also results in the directionality of foam rise already observed in Sect. 3.1. In comparison to other precursor materials, the shown samples made from a pre-alloyed AA6061 metal powder exhibit a rather homogeneous pore formation throughout the entire volume. The morphology of the metal matrix up to $\varepsilon = 0.44$ resembles "split wood" with solid "fibres" crossing rod-like or lens-like pores.

In order to investigate the evolution of pore morphology of this sample series quantitatively, we analyse the 3d images with respect to the volume fraction and the mean surface distribution of the pore space. Measurement of data is based on segmented[17] binary images of microstructural constituents representing the spatial distribution of the blowing agent (the TiH_2 particles) and the solid matter (the entire metallic matrix), respectively. Clearly, the binary image of the pore space is obtained be simple inversion of the binary image with respect to the solid matter.

The measurement of the volume fraction of the pores is based on counting of the voxels of the binary image concerning to the pore space. For the measurement of the specific surface area an integral-geometric approch is applied. In this approach[18,19] the translative and rotatory integral occuring in Crofton formula corresponding to the surface area is discretised where the discretisation is induced by the voxel lattice of the image. In Table 1 the volume fractions and specific surface areas of the pore space are given for the various expansion stages. With increasing foam expansion, the specific surface area of the pore space decreases since the pores inflate and transform after appearance of the liquid state from "split-wood"–like to a rounder, almost spherical shape.

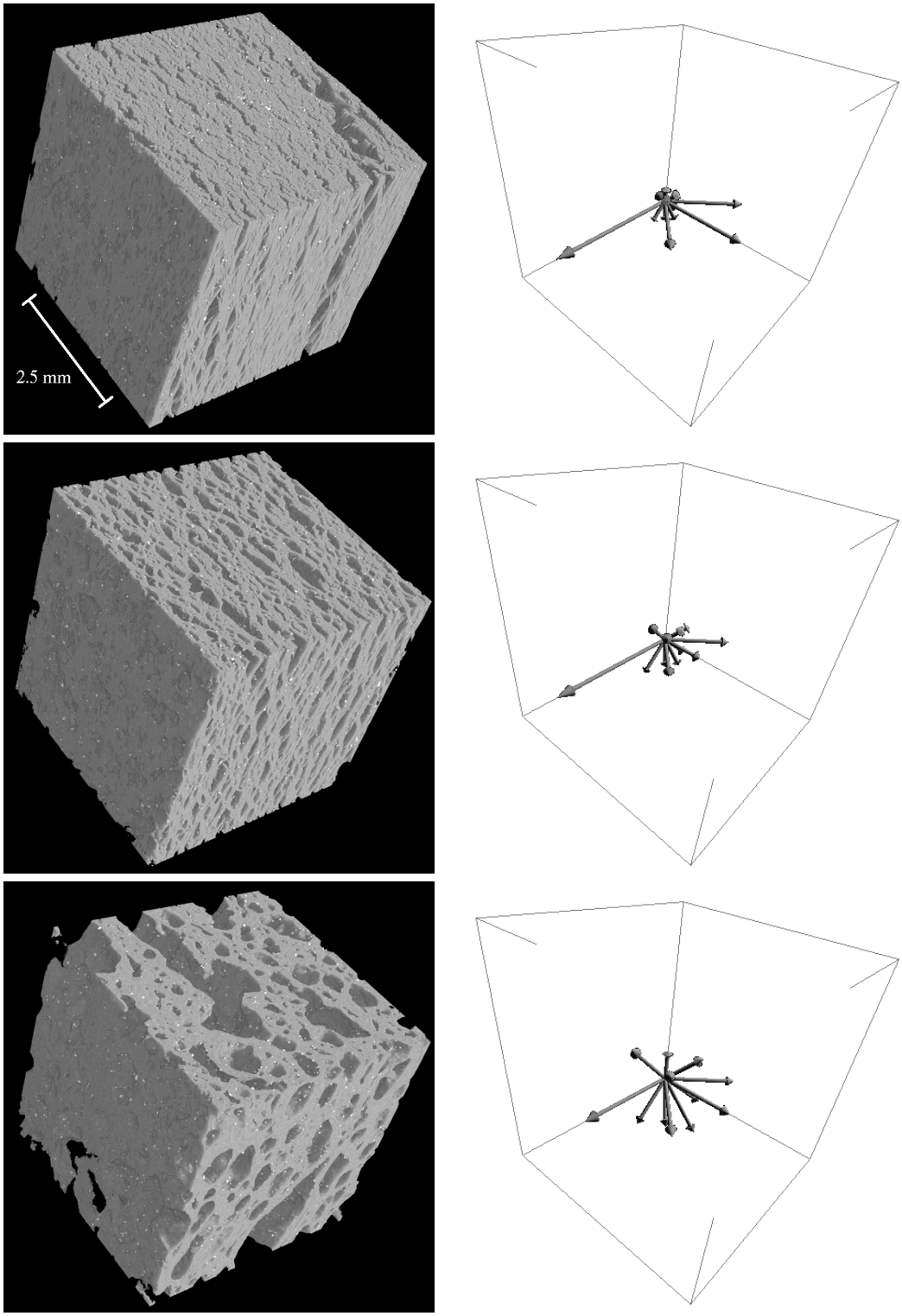

Figure 6. Left column: 3d renditions of different foam expansion stages for the AA6061 series (from top to bottom: $\varepsilon = 0.30, 0.44, 0.56$). The pore space is rendered transparent, the alloy matrix is grey and the remnants (mainly Ti) of the blowing agent particles are the light spots. Voxel size is $6.7\ \mu$m. Right column: Corresponding (discrete) directional distributions of the mean surface of the pore space.

The directional distribution of the mean surface is approximated by a discrete distribution on the unit sphere (see right column of Fig. 6). The lengths of the arrows shown in the diagrams is equivalent to the fraction of surface normal vectors corresponding to the arrows' directions. The two longest arrows of the top diagram correspond to the already noted rod-like pore shapes at $\varepsilon = 0.30$: almost no surface is oriented perpendicular to these two arrows (parallel to the up-down direction of the 3d rendition). The texture introduced by the powder compaction process (here extrusion) results in the observed strong biaxiality of the mean surface distribution. The extrusion process is characterised by a principal and a secondary compression axis which are defined by the aspect ratio of the extruded product of 160×20 mm^2 rectangular section. The longest arrow of each diagram is parallel to the principal axis of precursor compaction. In the second expansion stage $\varepsilon = 0.44$ the part of the surface with its normal oriented parallel to the principal compaction direction clearly dominates but with increasing expansion this dominance reduces considerable as the pores attain a more spherical shape. In summary, at early foaming stages the anisotropic pore morphology closely reflects the texture induced by the powder compaction step. With proceeding foam expansion, surface tension appearing in the semi-liquid state is thought to reduce gradually this anisotropy.

3.2.2. Spatial correlation between blowing agent and pores

One open question is where pores nucleate after the onset of hydrogen release by the blowing agent. Banhart *et al.*[20] investigated early foaming stages in Zn foam by scanning electron microscopy (SEM) and proposed two types of pore nucleation processes. The blowing gas released by a blowing agent particle could lead to *local pore formation* in the direct neighbourhood of the particle. SEM imaging, however, led to the conclusion that there exist pores with no blowing agent particle in their direct neighbourhood. It was suggested that such *non-local pore formation* often occurs at triple grain junctions in the polycrystalline Zn. Due to the 2d imaging approach employed to investigate the sample surface it could not be excluded, however, that not every blowing agent particle has been found in the spatial neighbourhood of the investigated pores.[20] Moreover, the sample preparation process for SEM might even had removed some of the particles. Since we can distinguish blowing agent particles from the metallic matrix and the pores we will investigate in the following this correlation quantitatively for aluminium alloys in 3d.

In order to measure numerically a characteristic describing the spatial correlation between pore nucleation and blowing agent particles' positions, the solid matter is sequentially eroded[17] using structuring elements of increasing size where morphological erosion applied to a binary image is analogous to maximum filtering and the structuring element corresponds to the support of the filter mask. Notice, we consider 3d erosion, *i.e.* the structuring element represents a spatial voxel set.

For large structuring elements (*i.e.* with increasing step number) the solid matter is completely removed from the binary image. By each of these erosion steps one defines pixels concerning to the solid matter having a defined distance from the pore space. More specifically, in the i–th step we consider all voxels of the solid matter not removed by (i-1)–th erosion step but elimimated by the i–th step (differential erosion volume). The voxels of the solid matter selected in the i–th step have well defined distances from the pore space where the definition of the distance depends on the choice of the sizes and shapes of the (discrete) structuring elements. Finally, we consider all voxels belonging to the TiH_2 constituent and to the solid matter detected in the i–th erosion step. The number of these voxels over the total number of the voxels detected in the i–th erosion step characterises the correlation between pores' and blowing agent particles' positions. If this fraction — considered as a function of the step number i — is independent from i then pore sites and sites of blowing agent particles are independent and thus no correlation exists. Fig. 7 plots the normalised volume fraction of TiH_2 in the differential erosion volume as a function of the erosion volume over the total volume, and as a constant over each erosion step i. The plots can thus be interpreted as profiles of the mean TiH_2 concentration with increasing distance from the pore space.

alloy	pixel size	macrosc. porosity ε	computed porosity	specific surface area in m^{-1}
AlSi7	0.7 μm	0.09	0.049	68053.8
AA6061	0.7 μm	0.01	0.027	34219.1
AA6061	6.7 μm	0.30	0.312	25381.9
AA6061	6.7 μm	0.44	0.407	16689.1
AA6061	6.7 μm	0.56	0.549	7721.3

Table 1. Computed characteristics of porosity and specific surface area of the pore space for the samples of macroscopic porosity ε.

Shown are two foam samples stemming from different precursor materials at the onset of foaming. Whereas for AA6061 a strong correlation is found, almost no correlation exists in the case of AlSi7. This disagrees with SEM observations[21] of an AlSi7 sample with 2 % expansion which indicated a spatial correlation of pores and blowing agent particles. The difference between the AA6061 and AlSi7 foam samples can be explained as follows. The foamable precursor material was fabricated in the case of AA6061 from a single pre-alloyed powder. Obviously, the pores nucleate locally at the interface between alloy and the blowing agent. In contrast, the AlSi7 precursor material is made from two powders to form the alloy during foaming. Pores are found to nucleate without correlation to the blowing agent particles' sites but presumably in the neighbourhood of the silicon powder particles which has already been indicated by the SEM investigations[21] mentioned above.

4. CONCLUSIONS

Process observations under thermal load are performed in real time by radiographic experiments. For the first time, the structural changes during foam expansion could be studied *in situ* by projection image sequences. Monochromatic radiation permits quantitative absorption imaging for the selected x-ray energy which has been exploited for the quantification of drainage. This allows us to draw the following conclusions: film rupture processes and drainage are in fact closely related for metallic foams due to the instability of metal films. The time scale of film ruptures must lie significantly below 50 ms in the case of Al alloy foams.

The tomographic experiments image the sample volume non-destructively in 3d. At the sample interior, the sample preparation has no detrimental effect on the constituents (*i.e.* the blowing agent particles). The application of SR yields highly contrasted reconstructions: monochromatic radiation permits the quantitative determination of the linear attenuation coefficient distribution and reduces reconstruction artefacts. Thus the pores, alloy matrix and blowing agent could be separated. Moreover, high spatial resolution allows us to resolve features at the micron scale.

SR microtomography was applied to investigate the early foam formation *ex situ* by imaging of sample series of different foam expansion stages. Dedicated 3d image processing and analysis techniques give access to the statistical distribution properties among the series. In particular, the 3d spatial correlation between blowing agent and pores could be determined. At the onset of foaming, pore nucleation is found to be different for two differently fabricated precursor materials. Moreover, the pore–matrix interface could be examined quantitatively which allows us to conclude on the temporal evolution of pore morphology during foaming. In the solid state, pore morphology closely reflects the anisotropic strength of the precursor material which is a result of the powder compaction step. After the transition to the semi-solid state, surface tension becomes dominant which reduces gradually the observed anisotropic pore morphology.

In summary, pore nucleation, pore formation and foam decay can be related by the described investigation methods to the precursor material, its fabrication steps and process parameters (*e.g.* temperature, ambient pressure *etc.*).

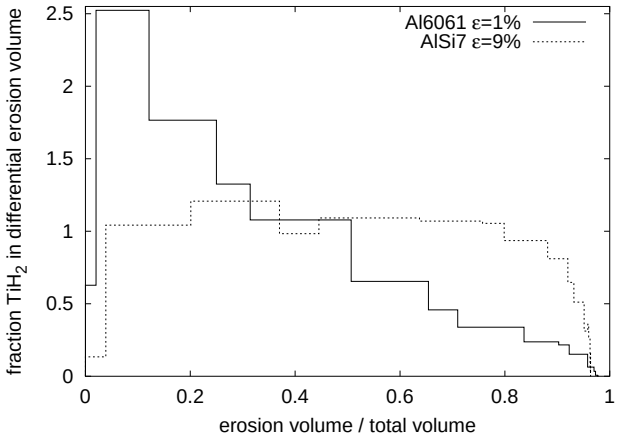

Figure 7. Spatial correlation between pores and blowing agent for the AA6061 expansion series (left: $6.7\ \mu$m voxel size) and for the two dense samples investigated with $0.7\ \mu$m voxel size (right). Plotted is the volume fraction of TiH_2 in the erosion volume on each erosion step, normalised to the mean blowing agent volume concentration. The computations were carried out on 3d data sets of 660^3 voxels.

ACKNOWLEDGEMENTS

The authors would like to thank the ESRF Topography and Imaging Group for their help. We acknowledge D. Fernandez and J.C. Labiche for their contributions to the acquisition set-ups.

REFERENCES

1. J. Banhart, "Manufacture, characterisation and application of cellular metals and metal foams," *Progr. Mater. Sci.* **46**, pp. 559–632, 2001.
2. A. Sassov, "Non-destructive 3-d investigation of metallic foam microstructures," *Adv. Eng. Mater.* **2**, pp. 466–470, 2000.
3. H. Bart-Smith, A.-F. Bastawros, D. Mumm, A. Evans, D. Sypeck, and H. Wadley, "Compressive deformation and yielding mechanisms in cellular al alloys determined using x-ray tomography and surface strain mapping," *Acta Mater.* **46**, pp. 3582–3592, 1998.
4. O. Olurin, M. Arnold, C. Körner, and R. Singer, "The investigation of morphometric parameters of aluminium foams using micro-computed tomography," *Materials Science and Engineering A* **328**, pp. 334–343, 2002.
5. L. Helfen, P. Cloetens, W. Ludwig, P. Pernot, and T. Baumbach, "New trends of microtomography and fast radiography for the real-time and in-situ characterization of microstructures," in *Proceedings SPIE: Testing, Reliability, and Application of Micro- and Nanomaterial Systems*, N. Meyendorf, G. Baaklini, and B. Michel, eds., **5045**, 2003.
6. P. Cloetens, W. Ludwig, E. Boller, L. Helfen, L. Salvo, R. Mache, and M. Schlenker, "Quantitative phase contrast tomography using coherent synchrotron radiation," in *Proceedings SPIE: Developments in X-Ray Tomography III*, U. Bonse, ed., **4503**, pp. 82–91, 2002.
7. T. Weitkamp, C. Rau, A. Snigirev, B. Benner, T. Günzler, M. Kuhlmann, and C. Schroer, "Phase contrast in synchrotron-radiation microradiography and tomography," in *Proceedings SPIE: Developments in X-Ray Tomography III*, U. Bonse, ed., **4503**, pp. 92–102, 2002.
8. J. Banhart, H. Stanzick, L. Helfen, and T. Baumbach, "Metal foam evolution studied by synchrotron radioscopy," *Appl. Phys. Lett.* **78**, pp. 1152–1154, 2001.
9. J. Banhart, H. Stanzick, L. Helfen, T. Baumbach, and K. Nijhof, "Real-time x-ray investigation of aluminium foam sandwich production," *Adv. Eng. Mater.* **3**, p. 407, 2001.
10. H. Stanzick, M. Wichmann, J. Weise, L. Helfen, T. Baumbach, and J. Banhart, "Process control in aluminium foam production using real-time x-ray radioscopy," *Adv. Eng. Mater.* **4**(10), pp. 814–823, 2002.
11. L. Helfen, T. Baumbach, H. Stanzick, J. Banhart, A. Elmoutaouakkil, and P. Cloetens, "Viewing the early stage of metal foam formation by computed tomography using synchrotron radiation," *Adv. Eng. Mater.* **4**(10), pp. 808–813, 2002.
12. C. Körner and R. Singer, "Processing of metal foams — challenges and opportunities," *Adv. Eng. Mater.* **2**, pp. 159–165, 2000.
13. I. Duarte and J. Banhart, "A study of aluminium foam formation — kinetics and microstructure," *Acta Mater.* **48**, pp. 2349–2362, 2000.
14. B. Kriszt, P. Cekan, and K. Faure, "Foamability of the Al-Si system," in *Cellular Metals and Metal Foaming Technology*, J. Banhart, M. Ashby, and N. Fleck, eds., *MIT Publishing* , pp. 77–82, 2001.
15. D. Weaire and S. Hutzler, *The physics of foams*, Oxford University Press, Oxford, 1999.
16. G. T. Herman, *Image Reconstruction from Projections*, Academic Press, New York, 1980.
17. K. Castleman, *Digital image processing*, Prentice-Hall International Inc., Englewood Cliffs, New Jersey, 1996.
18. J. Ohser and F. Mücklich, *Statistical Analysis of Microstructures in Materials Science*, J Wiley & Sons, Chichester, New York, 2000.
19. C. Lang, J. Ohser, and R. Hilfer, "On the analysis of spatial binary images," *J. Microscopy* **202**, pp. 1–12, 2001.
20. J. Banhart, D. Bellmann, and H. Clemens, "Investigation of metal foam formation by microscopy and ultra small-angle neutron scattering," *Acta Mater.* **49**, pp. 3409–3420, 2001.
21. U. Mosler, A. Müller, H. Baum, U. Martin, and H. Oettel, "Microstructure of foamable precursor and foamed aluminium material," in *Cellular Metals and Metal Foaming Technology*, J. Banhart, M. Ashby, and N. Fleck, eds., *MIT Publishing* , pp. 233–238, 2001.